



Numerical assessment of cavitation erosion risk using incompressible simulation of cavitating flows

Downloaded from: <https://research.chalmers.se>, 2021-08-31 11:53 UTC

Citation for the original published paper (version of record):

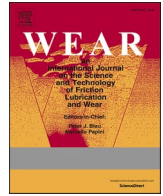
Arabnejad Khanouki, M., Svennberg, U., Bensow, R. (2021)

Numerical assessment of cavitation erosion risk using incompressible simulation of cavitating flows

Wear, 464-465

<http://dx.doi.org/10.1016/j.wear.2020.203529>

N.B. When citing this work, cite the original published paper.



Numerical assessment of cavitation erosion risk using incompressible simulation of cavitating flows

Mohammad Hossein Arabnejad^{a,*}, Urban Svennberg^b, Rickard E. Bensow^a

^a *Mechanics and Maritime Sciences, Chalmers University of Technology, 412 96, Gothenburg, Sweden*

^b *Kongsberg Maritime Sweden AB, 681 95, Kristinehamn, Sweden*

ARTICLE INFO

Keywords:

Cavitation
Cavitation erosion
Risk assessment
Incompressible simulation

ABSTRACT

In this paper, a numerical method to assess the risk of cavitation erosion is proposed, which can be applied to incompressible simulation approaches. The method is based on the energy description of cavitation erosion, which considers an energy transfer between the collapsing cavities and the eroded surface. The proposed framework provides two improvements compared with other published methods. First, it is based on the kinetic energy in the surrounding liquid during the collapse instead of the potential energy of collapsing cavities, which avoids the uncertainty regarding the calculation of the collapse driving pressure in the potential energy equation. Secondly, the approach considers both micro-jets and shock-waves as the mechanisms for cavitation erosion, while previous methods have taken into account only one of these erosion mechanisms. For validation, the proposed method is applied to the cavitating axisymmetric nozzle flow of Franc et al. (2011), and the predicted risk of cavitation erosion is compared with the experimental erosion pattern. This comparison shows that the areas predicted with high erosion risk agree qualitatively well with the experimental erosion pattern. Furthermore, as the current method can be used to study the relationship between the cavity dynamics and the risk of cavitation erosion, the hydrodynamic mechanism responsible for the high risk of cavitation erosion at the inception region of the sheet cavity is investigated in detail. It is shown for the first time that the risk of cavitation erosion in this region is closely tied to the separation of the flow entering the nozzle.

1. Introduction

Hydrodynamic cavitation is unavoidable in high-performance hydraulic machineries, such as propellers, water turbines, pumps, and diesel injectors. This phenomenon occurs when the pressure drop in an accelerating liquid flow leads to the formation of pockets of vapor, known as cavities. The collapse of these cavities near the surface is associated with a high mechanical load in the material, which can eventually lead to material loss and cavitation erosion. This material loss significantly increases operating costs of hydraulic machinery; therefore, it is essential to assess the risk of cavitation erosion in the design process. Traditionally, the cavitation erosion risk is assessed by applying experimental methods on the prototype of a newly designed machine. These experimental methods include visual assessment of collapsing cavities using high-speed videos [1] complemented by paint test and/or acoustic measurement [2,3,4]. Such experimental methods are, however, expensive and mostly used in the late stage of the design process. Therefore, numerical methods capable of assessing the risk of cavitation

erosion are an attractive alternative as they can be applied in the early stage of the design.

Owing to significant progress over the past decade, current numerical simulations of cavitating flows are capable of reproducing the large-scale cavity dynamics controlling cavitation erosion. With this capability, it has recently become feasible to develop methods that can predict the cavitation erosion risk based on numerical results. Several of such approaches have been proposed in the literature, and they can be categorized into two groups: methods based on compressible simulations or incompressible simulations. In the case of compressible simulation, the strength of collapse-induced shock-waves captured by a compressible simulation are analyzed to assess the risk of cavitation erosion. These methods have been applied mostly to high-speed cavitating flows where the time-scale of the flow is comparable to the time-scale of collapse-induced shock waves. Koukouvinis et al. [5] and Örley et al. [6] investigated cavitation erosion in high-speed cavitating flows in diesel injectors using compressible methods and investigated the hydrodynamic mechanisms leading to cavitation erosion. Mihatsch et al.

* Corresponding author.

E-mail address: mohammad.h.arabnejad@chalmers.se (M.H. Arabnejad).

<https://doi.org/10.1016/j.wear.2020.203529>

Received 27 April 2020; Received in revised form 13 October 2020; Accepted 27 October 2020

Available online 2 November 2020

0043-1648/© 2021 The Authors. Published by Elsevier B.V. This is an open access article under the CC BY license (<http://creativecommons.org/licenses/by/4.0/>).

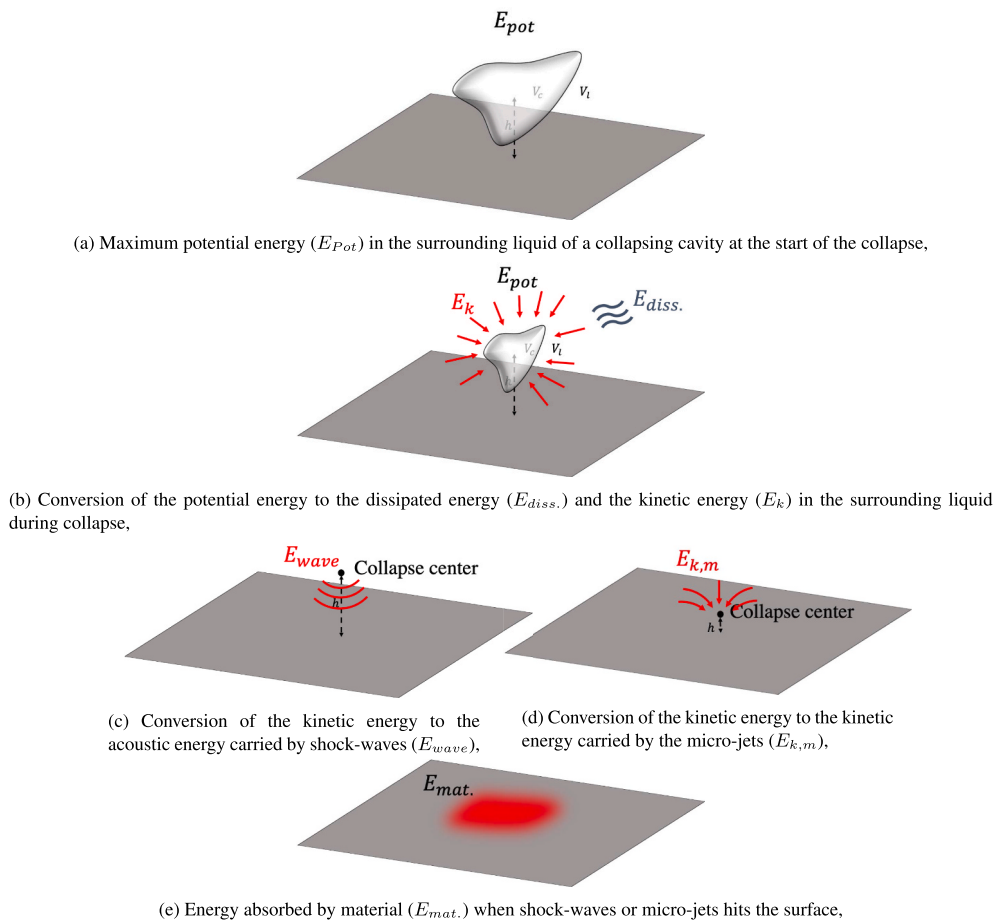


Fig. 1. Energy-based description of cavitation erosion.

[7] studied a cavitating flow in an axisymmetric nozzle with the aim to assess the risk of cavitation erosion. They showed that the areas predicted with high risk of cavitation erosion agree well with the experimental erosion pattern by Franc et al. [8]. Blume and Skoda [9] examined a high-speed cavitating flow over a hydrofoil with the aim to assess risk of cavitation erosion. Using the location of aggressive collapses and pressure peaks on the foil surface, they were able to predict the areas with high risk of cavitation erosion. It should be mentioned that compressible methods have been applied to low-speed cavitating flows around propellers and foils by Budich et al. [10,11] and Arabnejad et al. [12]. However, the simulations in these studies are inviscid due to the high computational cost of compressible methods for low-speed cavitating flows.

Alternatives to the above compressible approaches are methods where incompressible simulations are used to assess the risk of cavitation erosion. The aim then is to estimate the risk of cavitation erosion based on the flow properties in the simulation. Ochiai et al. [13] used a method where Lagrangian bubbles are injected in the simulation of cavitating flow, and the risk of cavitation erosion is assessed based on acoustic pressure emitted from these bubbles. Similarly, Peters and el Moctar [14] proposed an erosion assessment method based on Lagrangian bubbles present in a multi-scale Euler–Lagrange simulation of cavitating flows. Krumenacker et al. [15] developed a numerical erosion assessment using the acoustic energy of bubble/cavity implosion. This acoustic energy was obtained from Rayleigh-Plesset software which takes input from Eulerian simulation of cavitating flows. Li et al. [16] developed a method to assess the risk of cavitation erosion based on the accumulation of time derivative of pressure on the surface. The method was successfully applied to a cavitating flow over a foil; however, the predicted cavitation erosion risk by this method is highly

dependent on the threshold of the method according to Eskilsson and Bensow [17]. Alternatively, Koukouvinis et al. [18] proposed an erosion risk indicator as a function of the total derivative of pressure and vapor fraction which then was applied to the cavitating flow in the experiment of Franc et al. [8]. Dular et al. [19] developed a method to estimate the risk of cavitation erosion based on the micro-jet hypothesis. Peters et al. [20,21] proposed a similar method considering the micro-jet mechanism of cavitation erosion and applied the method to the cavitating flows around a ship propeller in model- and full-scale. Eskilsson and Bensow [17] compared three of the above mentioned numerical erosion indicator and concluded that further research is necessary to develop reliable numerical erosion assessment methods.

A sub-category of incompressible erosion assessment methods, which has been identified by Van et al. [22] to be more suitable for numerical erosion assessment, is based on energy description of cavitation erosion [1,23,24]. This description considers a balance between the risk of cavitation erosion and the potential energy of collapsing vapor structures, which is assumed to be proportional to the vapor content of collapsing cavity structures and the collapse driving pressure. Using the energy description of cavitation erosion, a few methods have been proposed [24,25] and applied [26,27,28] in the literature. All of these methods, however, possess the uncertainty regarding the definition of the collapse driving pressure, which is also noted by Schenke et al. [25]. According to Vogel and Lauterborn [29], the collapse driving pressure for a single collapsing bubble can be reasonably approximated by the pressure measured far from the collapse center; however, for complex unsteady cavitating flows with several cavities interacting with each other, it remains uncertain how this driving pressure should be obtained.

In this paper, a new numerical method to assess the risk of cavitation

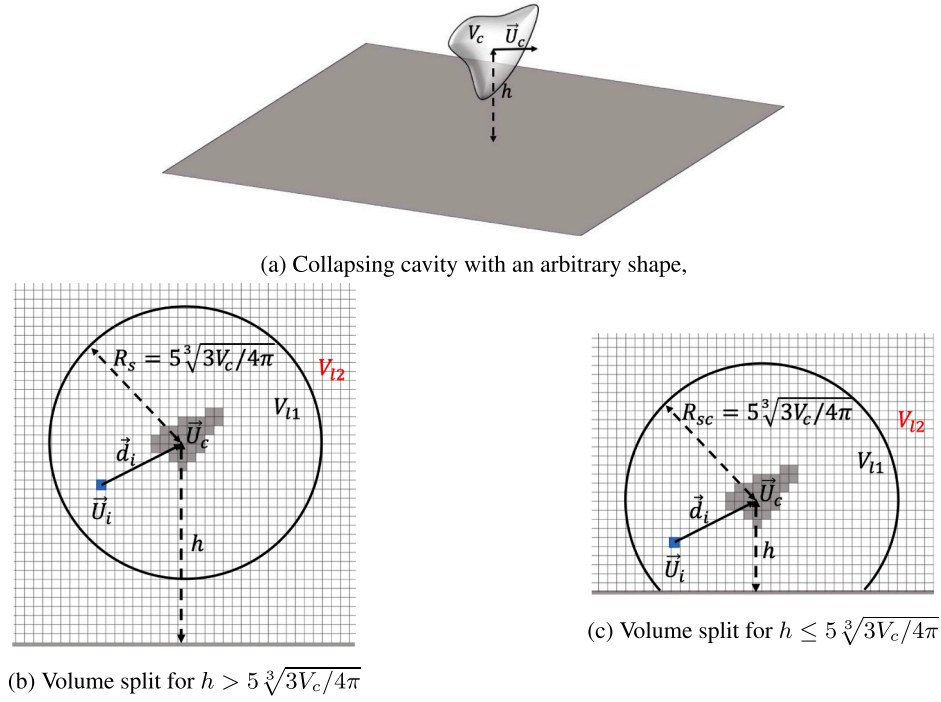


Fig. 2. Volume split of the surrounding liquid of a collapsing cavity.

erosion is presented. Similar to Fortes-Patella et al. [24] and Schenke et al. [25], the present method uses the energy balance between the collapsing cavities and cavitation erosion. However, in order to avoid the uncertainty regarding the definition of collapse driving pressure, the developed method is based on the kinetic energy in the surrounding liquid of collapsing cavities instead of the potential energy stored in these cavities. The method is then applied to a cavitating axisymmetric nozzle stagnation flow, and the erosion pattern obtained by the present method is compared with the experimental material removal by Franc et al. [8].

This paper is divided into five sections. Following this introduction, the developed method is presented starting with the theoretical framework of estimating the energy released by a collapsing cavity followed by some implementation details on how the cavity dynamics is traced leading to the erosion risk estimate. Then the numerical set-up and test case used for validation of the method are described. The results are presented including a detailed discussion on the cavitation development and the hydrodynamic mechanisms leading to erosion in this flow as well as the comparison between the predicted risk of cavitation erosion using the developed method and the experimental erosion pattern.

2. Estimation of erosion risk

The energy-based description of cavitation erosion caused by a macro-scale cloud cavity containing a large number of bubbles is shown in Fig. 1. This description suggests that when a macro-scale cloud cavity is created in the low-pressure region, the surrounding liquid gains potential energy (Fig. 1a). As this cloud cavity moves into the pressure recovery region and the collapse starts, most of the potential energy converts into the kinetic energy stored in the inward motion of the liquid while the rest dissipates away from the cavity (Fig. 1b). The dissipated energy can be in the form of the internal energy due to viscosity or acoustic energy when the shock-waves upon the collapse of bubbles in the boundary of the cloud cavity radiate away from the cavity. At the end of the collapse, depending on the distance between the cloud cavity and the nearby surface, the kinetic energy of the liquid is converted into acoustic energy carried by collapse-induced shock-waves as a result of bubbles collapsing away from the surface and/or focused into the micro-

jets due to the collapse of some bubbles near the surface (Fig. 1c and d). When these shock-waves or micro-jets hit the surface, a portion of their acoustic or kinetic energy is absorbed by the material (Fig. 1e). According to Fortes-Patella et al. [30], if the absorbed energy by the material exceeds a certain threshold, which is a function of material properties, cavitation erosion can occur. It can be noted from the energy-based description that the kinetic energy in the surrounding liquid of a collapsing cloud cavity is transferred to the nearby material, normally considered occurring through two mechanisms, shock-waves and micro-jets, at the level of bubble-scale. Capturing the detail of this energy transfer directly in engineering simulations is not computationally possible, both considering the very high mesh resolutions needed in the Eulerian approach as well as considering compressibility effects and its time scale. Here, we instead present the development of a framework which can model this energy cascade based on the flow quantities at the level of macro-scale cavities in the Eulerian incompressible simulation of cavitating flows. For this modeling, first the dynamics of collapsing macro-scale cavities are traced during the simulation and the kinetic energy in the surrounding liquid of these collapsing cavities is estimated. Then, a subgrid modeling is provided which determines the portion of this kinetic energy which is transmitted to the material surface either through an approximation of a pressure wave or a micro-jet. In the following subsections, first, the theoretical description of estimating this kinetic energy is presented and then the implementation of tracking the cavity dynamics and the erosion estimation is described.

2.1. Theoretical description of estimating the kinetic energy

The kinetic energy in the surrounding liquid of a collapsing cavity can be obtained from,

$$E_k = \int_{V_i} \frac{1}{2} \rho_l U_r^2 dV, \quad (1)$$

where V_i is the volume of the surrounding liquid, ρ_l is the liquid density, and U_r is the collapse-induced velocity in the surrounding liquid. The discretized form of equation (1) over a finite volume mesh can be written as,

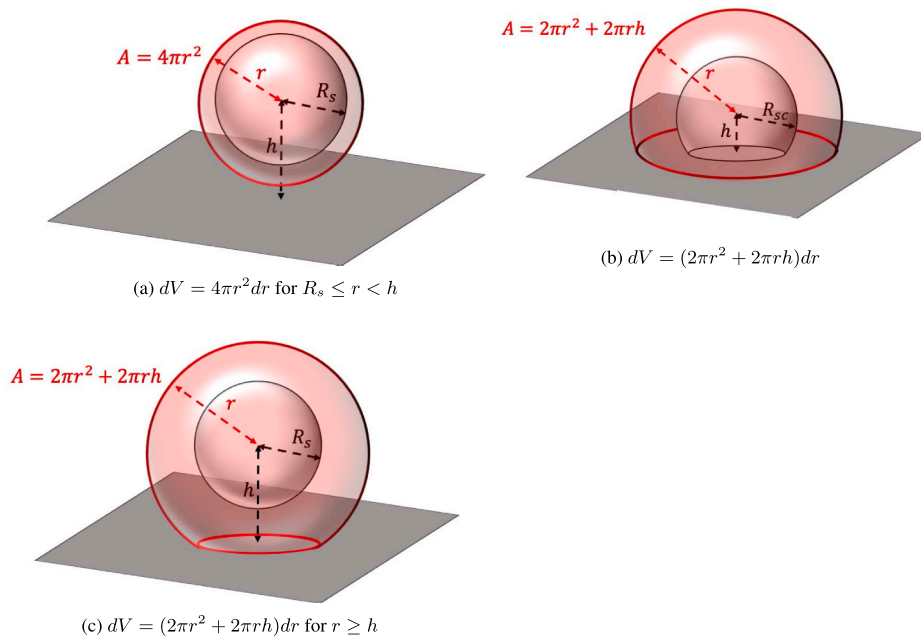


Fig. 3. Volume increments (red transparent sphere or spherical cap shells) used in the integration of the kinetic energy in far-field (the solid gray sphere or spherical cap represents the interface of the volume split shown in Fig. 2). (For interpretation of the references to colour in this figure legend, the reader is referred to the Web version of this article.)

$$E_k = \sum_{i \in V_l} \frac{1}{2} \rho_i V_i U_{r,i}^2, \quad (2)$$

where ρ_i and V_i are, respectively, the density and the volume of the cell i located in the surrounding liquid, and $U_{r,i}$ is the collapse-induced velocity in the cell i which can be obtained from,

$$U_{r,i} = \left(\vec{U}_i - \vec{U}_c \right) \cdot \vec{d}_i / |\vec{d}_i|. \quad (3)$$

In the above equation, \vec{U}_i is the velocity in the cell i , \vec{U}_c is the volume-averaged velocity of the cells containing the collapsing cavity, and \vec{d}_i is the vector connecting the centers of cell i and the center of collapsing cavity.

Using equation (2) to obtain the kinetic energy of the surrounding liquid requires a loop over the cells in the entire domain at each time step for each collapsing cavity which is computationally expensive. As a remedy for this high computational cost, the surrounding liquid of a

error related to approximating the kinetic energy in the far-field volume. It should be mentioned that the sensitivity of the predicted risk of cavitation erosion to the chosen value for the radius of the sphere or the spherical cap is examined in the results section. Based on the volume split, the kinetic energy in the surrounding liquid is split into the near-field kinetic energy, $E_{k,1}$, and the far-field kinetic energy, $E_{k,2}$,

$$E_k = E_{k,1} + E_{k,2}. \quad (4)$$

The near-field kinetic energy can be obtained directly from equation (2) while the far-field kinetic energy, $E_{k,2}$ is approximated with the assumption that the collapse-induced velocity in the far-field volume, U_r , is only a function of the distance from the center of the cavity, r . It should be mentioned that this assumption is true for a cavity with arbitrary shape if the distance from the cavity center is significantly larger than the characteristic length of the cavity. Applying this assumption and using the volume increments, dV , in Fig. 3a, b, and c, $E_{k,2}$ can be approximated as

$$E_{k,2} = \int_{V_2} \frac{1}{2} \rho_l U_r^2 dV \approx \begin{cases} \int_{R_s}^h \frac{1}{2} \rho_l U_r^2 (4\pi r^2) dr + \int_h^\infty \frac{1}{2} \rho_l U_r^2 (2\pi r^2 + 2\pi r h) dr & h > 5 \sqrt[3]{3V_c/4\pi} \\ \int_{R_{sc}}^\infty \frac{1}{2} \rho_l U_r^2 (2\pi r^2 + 2\pi r h) dr & h \leq 5 \sqrt[3]{3V_c/4\pi} \end{cases}, \quad (5)$$

collapsing cavity is split into two volumes, a near-field volume and far-field one. The near-field volume, V_{n1} in Fig. 2b and c, includes the liquid inside the sphere or spherical cap with radius five times larger than the radius of the sphere with the same volume of the collapsing cavity while the far-field volume, V_{f2} in Fig. 2b and c, contains the liquid outside of this sphere or spherical cap. The choice of the radius of the sphere or the spherical cap is somewhat arbitrary, balancing that choosing a larger near-field volume increases the computational cost of the method, compromising the applicability of the current method in an industrial application while selecting a smaller near-field volume may increase the

where R_s and R_{sc} are, respectively, the radius of the sphere and spherical cap, shown in Fig. 2b and c, and h is the normal distance between the center of the cavity and the nearest wall. To be able to compute the above integral, the distribution of the collapse-induced radial velocity, U_r , should be estimated. The continuity equation for the mixture enclosed by the volume increments in Fig. 3a, b, and c gives,

$$U_r \rho_l A = \dot{V}_v (\rho_l - \rho_v), \quad (6)$$

where A is the surface area of the volume increment and \dot{V}_v is the time

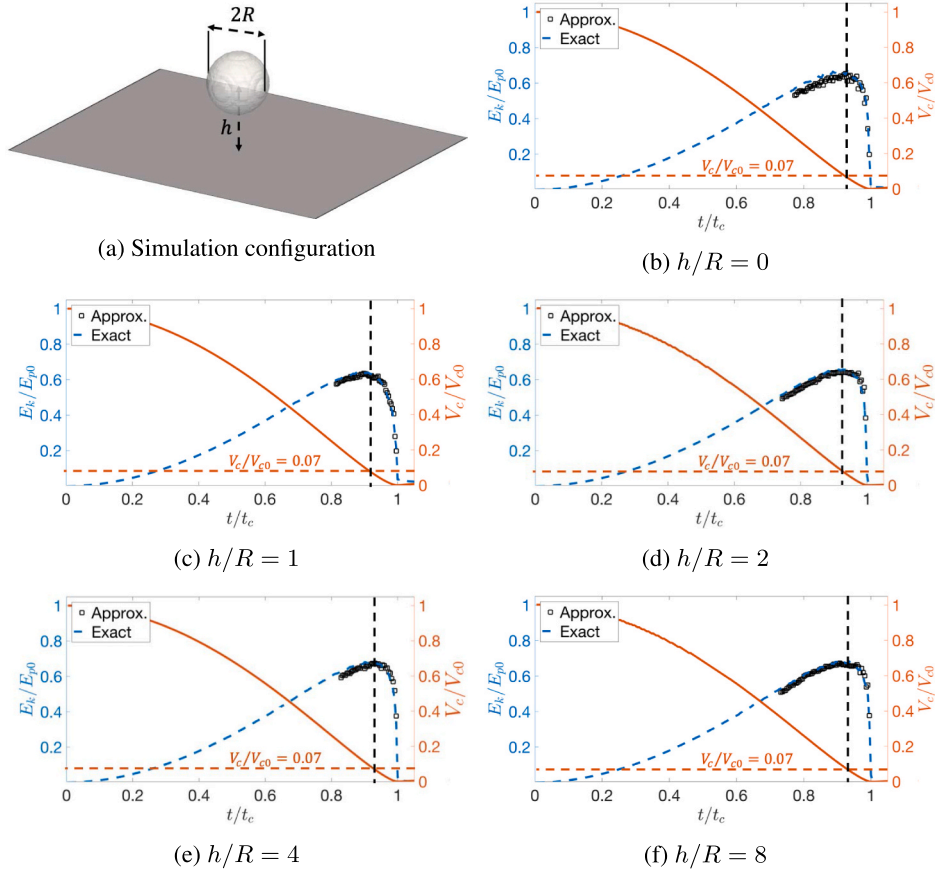


Fig. 4. Simulation of collapsing spherical mixture cloud cavities (a) simulation configuration, (b–f) the ratio between the kinetic energy in the surrounding liquid and the initial potential energy and the ratio between the cavity volume and the initial volume of the cavity as a function of time during the collapse.

derivative of vapor content in the cloud cavity. Note that the left hand side of equation (6) is the liquid mass flux across the volume increment and the right hand side is the mass transfer rate inside the volume increment. Assuming that $\rho_l \gg \rho_v$ and substituting the definition of surface areas A in Fig. 3a, b, and c, the distribution of induced radial velocity can be obtained from,

$$U_r = \begin{cases} \frac{\dot{V}_v}{4\pi r^2} & \text{for } R_s \leq r < h; \\ \frac{\dot{V}_v}{2\pi r^2 + 2\pi r h} & \text{for } r \geq h \quad h > 5\sqrt[3]{3V_c/4\pi} \\ \frac{\dot{V}_v}{2\pi r^2 + 2\pi r h} & h \leq 5\sqrt[3]{3V_c/4\pi} \end{cases} \quad (7)$$

Substituting the above equation in equation (5) and evaluating the integral gives the far-field kinetic energy as,

$$E_{k,2} \approx \begin{cases} \rho_l \dot{V}_v^2 \left(\frac{1}{8\pi R_s} - \frac{1}{8\pi h} + \frac{\ln(2)}{4\pi h} \right) & h > 5\sqrt[3]{3V_c/4\pi} \\ \rho_l \dot{V}_v^2 \left(\frac{1}{4\pi h} \right) \ln \left(\frac{h + R_{sc}}{R_{sc}} \right) & h \leq 5\sqrt[3]{3V_c/4\pi} \end{cases} \quad (8)$$

Using equations (2), (4) and (8), the final form of the kinetic energy in the surrounding liquid can be written as,

$$E_k \approx E_{k,1} + E_{k,2} = \sum_{i \in V_{l1}} \frac{1}{2} \rho_i V_i U_{r,i}^2 + \begin{cases} \rho_l \dot{V}_v^2 \left(\frac{1}{8\pi R_s} - \frac{1}{8\pi h} + \frac{\ln(2)}{4\pi h} \right) & h > 5\sqrt[3]{3V_c/4\pi} \\ \rho_l \dot{V}_v^2 \left(\frac{1}{4\pi h} \right) \ln \left(\frac{h + R_{sc}}{R_{sc}} \right) & h \leq 5\sqrt[3]{3V_c/4\pi} \end{cases} \quad (9)$$

In order to validate the modeling presented above, a series of collapsing spherical mixture cloud cavities with different distances from the wall is simulated. The vapor fraction in these mixture clouds is initialized using a Gaussian distribution with the maximum vapor fraction of 0.8 at the center of the cloud. Using this method of initialization, the resultant clouds represent cloud cavities in the homogeneous mixture approach which are obtained by volume averaging spherical clouds of bubbles on a coarse mesh. The series of simulations consists of variations in different ambient pressure, $p_\infty = [1, 2, 3, 4, 10]$ bar; initial radius $R_0 = [2, 4, 8]$ mm; and initial vapor content, $V_{v,0} = [4.23 \times 10^{-7}, 8.42 \times 10^{-7}, 1.71 \times 10^{-6}] m^3$. The results are consistent for all conditions and we here limit the presentation to Fig. 4 and the mixture cloud cavity with $p_\infty = 10$ bar, $R_0 = 8$ mm, and $V_{v,0} = 1.71 \times 10^{-6} m^3$. For each collapsing cavity, the exact instantaneous kinetic energy is obtained by summing the kinetic energy in the cells of the computational domain, and the approximate kinetic energy is calculated by equation (9). Fig. 4 shows the evolution of the ratio between the kinetic energy in the surrounding liquid, obtained by both exact and approximate formulations during the collapse, and the initial potential energy, $E_{p0} = p_\infty V_{v,0}$. The comparisons between the exact and approximate formulation indicate that the approximate kinetic energy agrees well with the exact one. It can also be seen that when the collapse starts, the collapse-induced kinetic energy in the surrounding liquid increases progressively. This kinetic energy reaches its maximum, around 65% of the initial potential energy, before the end of the collapse and suddenly decreases to almost zero at the end of the collapse. It should be mentioned that the 35% of the potential energy which is not converted to the kinetic energy is dissipated due to viscous effects. As collapse proceeds, the velocity gradient in the surrounding liquid becomes very high. This high gradient then activates the viscous terms in the momentum equations which are

CavityNew 1	1	0	0	· · ·	0
CavityNew 2	0	1	1	· · ·	1
CavityNew 3	0	1	1	· · ·	0
·	·	·	·	·	·
·	·	·	·	·	·
·	·	·	·	·	·
CavityNew n	0	1	0		1
	CavityOld 1	CavityOld 2	CavityOld 3	· · ·	CavityOld m

Fig. 5. A schematic view of the *overlap-table*.

responsible for the dissipation of the potential energy. It is also interesting to note that regardless of the distance between the wall and the cavity, the ratio between the volume of the cavity at maximum kinetic energy and the initial volume of the cavity is 0.07. This value will be used later to determine which mechanism of cavitation erosion, micro-jet or shock-wave, is important.

2.2. Implementation of the method

According to the energy approach shown in Fig. 1, the maximum kinetic energy near the end of collapse, $E_{k,max}$, is focused to the material through shock-wave or micro-jet mechanism; therefore $E_{k,max}$ should be used to estimate the aggressiveness of collapsing events. However, obtaining this maximum kinetic energy for each collapsing cavity requires that the cavity is tracked up to its eventual collapse as $E_{k,max}$ occurs before the end of collapse (shown in Fig. 4). In the following sections, the algorithms used for detecting the collapsing cavities in each time step and tracking them between consecutive time steps are explained.

2.2.1. Detecting collapsing cavities

The algorithm used to identify collapsing cavities is similar to the one used by Vallier [31]. At each time step, a list of cells with vapor fraction, α^v , larger than a threshold ($\alpha^v > 0.01$) and negative total time derivative of vapor content ($\dot{V}_v < 0.0$) is created. The latter condition simply implies that the collapse has been initiated in these cells. The algorithm goes through this list and extracts the collapsing cavities from the cells in the list that are neighbours. In order to reduce the computational cost of the implemented tool, the collapsing cavities are detected close to their eventual collapse, when all of the cells containing the cavity have a negative total time derivative of vapor content. For each detected collapsing cavity, i , the kinetic energy in the surrounding liquid, $E_{k,i}$, is obtained from equation (9). The volume of the cavity, V_i , and the cavity center of volume, C_i , are also calculated from,

$$V_i = \sum_{j=1}^k V_{cell,j} \quad (10)$$

$$C_i = \frac{\sum_{j=1}^k C_{cell,j} V_{cell,j}}{V_i} \quad (11)$$

where k is the number of cells containing the collapsing cavity and $V_{cell,j}$ and $C_{cell,j}$ are, respectively, the volume and the center of the cell j .

2.2.2. Cavity tracking

In order to track the collapsing cavities between consecutive time steps, the cavity extracted in the previous section are stored in a list called *cavityListNew*. The collapsing cavities in the previous time step are also kept and stored in a list called *cavityListOld*. The main task in tracking the cavities is to find a best match for a collapsing cavity in *cavityListNew* from *cavityListOld*. The methodology for finding the best match is based on overlap detection and it is similar to the one presented in Silver and Wang [32]. In each time step, a table called *overlap-table* is created by checking the overlap between cavities in *cavityListNew* and *cavityListOld*. A schematic view of the *overlap-table* is shown in Fig. 5. The table has m rows and n columns where m and n are, respectively, the size of *cavityListNew* and *cavityListOld*. Initially, the values in the table are set to zero. After the overlap detection, the value stored in the row i and column j of this table is set to 1 if the i th cavity in *cavityListNew* overlaps with the j th cavity in *cavityListOld*. Based on the non-zero values in *overlap-table*, the following events can be detected.

- **Creation:** If all of the values in row i are zero, the cavity i in *cavityListNew* does not overlap with any cavity in *cavityListOld*, therefore it is a newly detected collapsing cavity. For this cavity, the maximum kinetic energy in the surrounding liquid, $E_{k,max,i}$, is equal to the kinetic energy calculated from equation (9).
- **Continuation:** If the value in row i and column j is one while other values in the row and the column are zero, the cavity i in *cavityListNew* and the cavity j in *cavityListOld* overlap only with each other. In this case, the cavity i is the continuation of the cavity j . The maximum kinetic energy of cavity i , $E_{k,max,i}$, is then obtained from,

$$E_{k,max,i} = \max(E_{k,max,j}, E_{k,i}), \quad (12)$$

where $E_{k,i}$ is the instantaneous kinetic energy of the cavity i and $E_{k,max,j}$ is the maximum kinetic energy of the cavity j .

- **Merge/Break up:** If there are several non-zero values in the row i , it is assumed that several cavities in *cavityListOld* have merged together and formed the cavity i in *cavityListNew*. Similarly, if there exists more than one non-zero values in the column j , it is assumed that the cavity j in *cavityListOld* has broken up into several cavities in *cavityListNew*. In both cases, the cavities in *cavityListNew* formed by break-up or merge are treated as newly detected collapsing cavities, therefore the maximum kinetic energy in the surrounding liquid, $E_{k,max,i}$, is equal to the kinetic energy calculated from equation (9).
- **Collapse:** If all of the values in column j are zero, the cavity j in *cavityListOld* does not have overlap with any cavities in *cavityListNew*. It is then assumed that the cavity j in *cavityListOld* has collapsed in the new time step.

For each collapsed cavity detected by the above algorithm, the collapse locations, C_i , the maximum kinetic energy, $E_{k,max,i}$, and the volume of the cavity at maximum kinetic energy, $V_{k,max,i}$, are written out as the output of the cavity tracking algorithm.

2.2.3. Indicator of cavitation erosion risk

Based on the energy approach, the kinetic energy in the surrounding liquid of collapsing cavities is transferred to the nearby material by shock-wave or micro-jet mechanisms. These collapsing cavities are mostly cloud of bubbles which are transported to high-pressure regions by the flow. For the cloud cavities collapsing far from the surface, the collapse of the bubbles inside the cloud produce shock-waves, therefore it can be assumed that the kinetic energy in the surrounding liquid is converted to acoustic energy carried by the collapse-induced spherical shock-waves. When these shock-waves hit the surface, a fraction of their acoustic energy is transferred to the surface. This fraction is estimated by Leclercq et al. [33] using a discrete solid angle projection on a triangular surface element. Similarly, Schenke and van Terwisga [34] introduced a

continuous form of the solid angle projection, which does not require the projection on triangular surface elements. Using this continuous form, the amount of energy absorbed by a surface element j due to the collapsing cavity i can be calculated from,

$$E_{mat,j} = \frac{1}{4\pi} \left(\frac{\vec{d}_{ij} \cdot \vec{n}_j}{|\vec{d}_{ij}|^3} \right) A_j E_{ac,i}, \quad (13)$$

where $E_{mat,j}$ is the energy absorbed by the surface element j , \vec{d}_{ij} is the vector connecting the center of the collapse and the center of the surface element, \vec{n}_j is the normal unit vector of the surface element, A_j is the area of the surface element and $E_{ac,i}$ is the acoustic energy in the shock-wave due to the collapse. Note that in equation (13), collapse-induced shock-waves are assumed to decay according to linear acoustic theory, which is inline with the work by Johnsen and Colonius [35] who investigated the collapse of gas bubbles using a compressible solver. For the collapsing cavities on the surface, the bubbles inside the cavities undergo non-spherical collapse leading to the formation of micro-jets. For these cavities, it can be then assumed that the kinetic energy in the surrounding liquid converts to the kinetic energy carried by micro-jets, $E_{km,i}$. This kinetic energy is assumed to be uniformly transferred to the surface, which is hit by the micro-jets. For the collapsing cavity i , the surface includes the surface elements that are covered by the approximate projected area of the cavity on the nearby surface, $A_{proj,i}$. This area can be obtained from,

$$A_{proj,i} = \pi \left(\frac{3V_{0,i}}{4\pi} \right)^{2/3} \quad (14)$$

where $V_{0,i}$ is the initial volume of the cavity i which can be approximated by $V_{0,i} = (1.0/0.07)V_{k,max,i}$ according to Fig. 4. Using the above assumptions, the amount of energy absorbed by a surface element j due to the cavity i collapsing near the surface can be calculated from,

$$E_{mat,j} = \begin{cases} \frac{E_{km,i} A_j}{A_{proj,i}} & |d_{i,j}| < \sqrt{\left(\frac{3V_{0,i}}{4\pi} \right)^{2/3} + h_{i,j}^2} \\ 0 & |d_{i,j}| \geq \sqrt{\left(\frac{3V_{0,i}}{4\pi} \right)^{2/3} + h_{i,j}^2} \end{cases}, \quad (15)$$

where $h_{i,j}$ is the normal distance between the collapse center of cavity i and the surface element j , and $E_{km,i}$ is the kinetic energy stored in the micro-jet.

To determine which mechanism is dominant for collapsing cloud cavities, simulations or experimental investigations of collapsing clouds of bubble with different distances from the wall are needed. These simulations or experimental investigations are not available in the literature and performing them is out of scope of this paper; therefore in the present work, we follow the works by Ochiai et al. [13] and Dular et al. [36] on collapsing single bubbles near the surface. These authors concluded that the mechanism for cavitation erosion for collapsing bubbles depends on the initial stand-off ratio, γ , of the bubbles which is defined as,

$$\gamma = h / \sqrt{33V_0/4\pi} \quad (16)$$

where h is the distance between the bubble and the wall and V_0 is the initial volume of the bubble. The simulations by Ochiai et al. [13] have shown that for the bubbles with $\gamma \geq 3.0$, the collapse is almost spherical,

and the collapse-induced high pressure on the surface is generated by spherical shock-waves. Similarly, it is assumed here that for the cavities with $\gamma \geq 3.0$, the collapse of these cavities produce only shock-waves and the kinetic energy in the surrounding liquid of these collapsing cavities is converted to acoustic energy of the shock wave ($E_{ac,i} = E_{k,max,i}$). The energy absorbed by the material due to collapse of these cavities is then obtained from equation (13). For the collapsing bubble on the wall ($\gamma = 0.0$), Dular et al. [36] showed that cavitation erosion is solely caused by the micro-jet. Here, we assume that the same is true for the collapsing cavities on the surface, therefore the kinetic energy in the surrounding liquid is assumed to be focused to the kinetic energy of the micro-jet ($E_{km,i} = E_{k,max,i}$) and that equation (15) is used to obtain the energy absorbed by the surface. For cloud cavities with $0 < \gamma < 3.0$, it is assumed that a number of bubbles in these clouds, n_s , collapse away from the surface leading to the formation of shock-waves while the rest collapse near the surface and produce micro-jets. For the bubbles collapsing away from the surface, a portion of the acoustic energy carried by the collapse-induced shock-waves is transmitted away from the cloud cavity which can cause erosion. The rest of this acoustic energy is transferred back into the cloud cavity due to acoustic interaction leading to a higher driving pressure for the bubbles collapsing near the surface. Using these assumptions, the distribution of the kinetic energy between the shock-wave and micro-jet mechanisms for collapsing cavities with $0 < \gamma < 3.0$ can be written,

$$E_{ac,i} = \beta \frac{n_s}{n_t} E_{k,max,i}, \quad E_{km,i} = \left(1 - \beta \frac{n_s}{n_t} \right) E_{k,max,i}, \quad (17)$$

where β is the portion of acoustic energy transmitted away from the cloud cavity and n_t is the total number of bubbles inside the cloud. To obtain the exact distribution of the kinetic energy between the two erosion mechanisms from the above equation, $\frac{n_s}{n_t}$ and β should be known as the function of the initial stand-off ratio, γ , which requires a detailed investigation of collapsing clouds of bubbles with different distances from the wall. As mentioned earlier, this detailed investigation is not available in the literature; therefore, we simply assume that $\beta \frac{n_s}{n_t}$ changes linearly with γ with the conditions,

$$\begin{cases} \beta \frac{n_s}{n_t} = 1.0 & \text{if } \gamma = 3.0 \\ \beta \frac{n_s}{n_t} = 0.0 & \text{if } \gamma = 0.0 \end{cases}. \quad (18)$$

To discuss the implication of the above mentioned linear assumption, we consider a cloud cavity with $\gamma = 1.0$ and assume that half of the acoustic energy produced by the collapsing bubbles away from the surface in this cloud is absorbed by the bubbles collapsing near the surface ($\beta = 1/2$). With this assumption, the assumed linear distribution indicates that 2/3 of the collapsing bubbles produce shock-waves while the rest produce micro-jets. We remark that the bubbles forming micro-jets are not restricted to bubbles which are near the wall at the beginning of the collapse. According to the simulation by Ma et al. [37], due to the non-uniform distribution of the pressure around the cloud collapsing near a wall, a jet like motion forms toward the wall which pierces the cloud. This jet brings bubbles from the location away from the wall to the regions near the wall leading to a larger number of bubbles producing micro-jets. Substituting the linear distribution of $\frac{n_s}{n_t}$ based on the conditions in equation (18) into equation (17), the kinetic energy in the surrounding liquid is divided between the kinetic energy in the micro-jet and the acoustic energy of the shock-wave based on the stand-off distance of the cavity as,

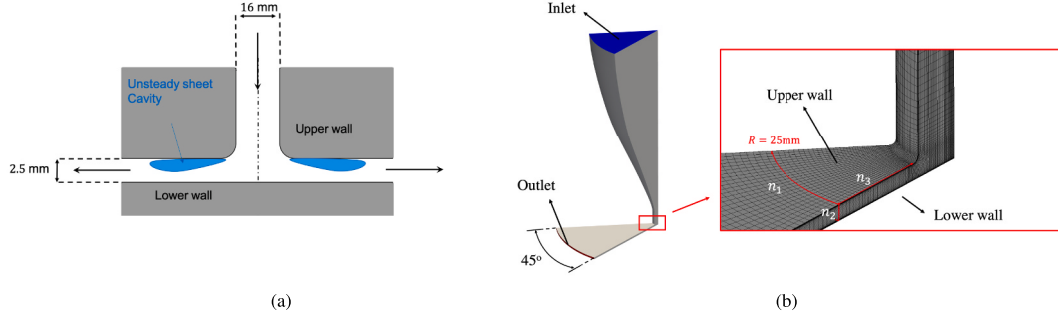


Fig. 6. Configuration for an axis-symmetric nozzle stagnation flow, a) schematic view of the configuration and the expected cavitation pattern seen in the experiment, b) Computational domain and mesh topology.

$$E_{km,i} = \left(1 - \frac{\gamma}{3.0}\right) E_{k,max,i}, \quad E_{ac,i} = \frac{\gamma}{3.0} E_{k,max,i}, \quad (19)$$

and the absorbed energy by the surface element, j , is obtained from,

$$E_{mat,j} = \frac{1}{4\pi} \left(\frac{\vec{d}_{i,j} \cdot \vec{n}_j}{|\vec{d}_{i,j}|^3} \right) A_j E_{ac,i} + \begin{cases} \frac{E_{km,i} A_j}{A_{proj,i}} & |d_{i,j}| < \sqrt{\left(\frac{3V_{0,i}}{4\pi}\right)^{2/3} + h_{i,j}^2} \\ 0 & |d_{i,j}| \geq \sqrt{\left(\frac{3V_{0,i}}{4\pi}\right)^{2/3} + h_{i,j}^2} \end{cases}. \quad (20)$$

According to the experimental study by Okada et al. [38] and the numerical study by Fortes-Patella et al. [30], there is a linear relationship between the volume loss due to cavitation erosion after the incubation period and the total energy stored in the eroded surface. Using this linear relationship, an indicator of cavitation erosion risk for the surface element, j , can be defined as,

$$EI_j = \frac{1}{t_s} \sum_{i=1}^{n_i} \frac{E_{mat,j,i}}{A_j}, \quad (21)$$

where t_s is the simulation time and n_i is the number of collapse events detected during the simulation. It should be noted that in equation (21), the total absorbed energy is divided by the simulation time and the area of the surface element to make the defined erosion indicator independent of these two parameters.

3. Numerical set-up

The above method is implemented in a modified version of the interPhaseChangeFoam solver from the OpenFOAM-2.2. x framework [39]. The solver has been validated and used to study cavitating flows by Bensow and Bark [40], and Asnaghi et al. [41]. The governing equations are the incompressible Navier Stokes equations for two-phase (liquid-vapor) isothermal flows. Using the homogeneous mixture assumption and applying LES low pass filter [42], the filtered equations for the mixture of liquid-vapor can be written as,

$$\frac{\partial}{\partial t}(\bar{\rho}) + \nabla \cdot (\bar{\rho} \bar{\mathbf{u}}) = 0, \quad (22)$$

$$\frac{\partial}{\partial t}(\bar{\rho} \bar{\mathbf{u}}) + \nabla \cdot (\bar{\rho} \bar{\mathbf{u}} \otimes \bar{\mathbf{u}}) + \nabla \cdot ([\bar{\rho} \mathbf{I} - \bar{\boldsymbol{\tau}}]) + \nabla \cdot (\boldsymbol{\tau}_{sgs}) = 0, \quad (23)$$

where $\bar{\rho}$, $\bar{\mathbf{u}}$, and \bar{p} are, respectively, the phasic filtered density, the Favre phasic filtered velocity vector, and the phasic filtered pressure, \mathbf{I} is the identity tensor, $\bar{\boldsymbol{\tau}}$ is the viscous stress tensor and $\boldsymbol{\tau}_{sgs}$ is the sub-grid scale tensor in the mixture momentum equations. Adopting the homogeneous mixture assumption and assuming that dynamic viscosity in each phase, μ^k , is constant, the mixture viscous stress tensor, $\bar{\boldsymbol{\tau}}$, can be obtained from,

$$\bar{\boldsymbol{\tau}} = \left(\sum_{k=1}^2 \alpha^k \mu^k \right) \bar{\mathbf{S}}, \quad (24)$$

where $\bar{\mathbf{S}}$ is the mixture strain tensor. To account for the effect of the sub-grid scale turbulence, we adopted the wall-adapting local eddy-viscosity (WALE) model proposed by Nicoud and Ducros [43]. In this model, the sub-grid scale tensor, $\boldsymbol{\tau}_{sgs}$, is written as,

$$\boldsymbol{\tau}_{sgs} = \frac{2}{3} k_{sgs} \mathbf{I} = -2\nu_{sgs} \bar{\mathbf{S}}, \quad (25)$$

where k_{sgs} is the sub-grid kinetic energy and ν_{sgs} is the sub-grid scale turbulent viscosity which can be obtained from,

$$\nu_{sgs} = C_k \Delta \sqrt{k_{sgs}}. \quad (26)$$

In the above equation, Δ is the cell length scale, C_k , the model constant, is assumed to be 1.6 and k_{sgs} , the sub-grid kinetic energy, can be calculated from,

$$k_{sgs} = \left(\frac{C_w^2 \Delta}{C_k} \right)^2 \frac{(\tilde{S}^d \tilde{S}^d)^3}{\left((\tilde{S} \tilde{S})^{5/2} + (\tilde{S}^d \tilde{S}^d)^{5/4} \right)^2}, \quad (27)$$

where \tilde{S} and \tilde{S}^d are, respectively, the resolved-scale strain rate tensor and traceless symmetric part of the square of the velocity gradient tensor, and C_w , the model constant, is assumed to be 0.325. The cavity dynamics is captured by Transport Equation Modeling (TEM), where a transport equation for the liquid volume fraction, α^l , is solved. This equation reads,

$$\frac{\partial}{\partial t}(\alpha^l \bar{\rho}^l) + \nabla \cdot (\alpha^l \bar{\rho}^l \bar{\mathbf{u}}) = \dot{m}, \quad (28)$$

where \dot{m} is the mass transfer term which accounts for vaporization and condensation. Here, the Schnerr-Sauer model [44] is used for this term. The mass transfer term is written as the summation of condensation, \dot{m}_{dc} , and vaporization, \dot{m}_{dv} , terms as,

$$\dot{m} = \alpha^l (\dot{m}_{dc} - \dot{m}_{dv}) + \dot{m}_{dc}, \quad (29)$$

where \dot{m}_{dv} and \dot{m}_{dc} are obtained from,

$$\dot{m}_{dc} = C_c \alpha^l \frac{3\bar{\rho}^l \bar{\rho}^v}{\bar{\rho} R_B} \sqrt{\frac{2}{3\bar{\rho}^l}} \sqrt{\frac{1}{|\bar{p} - p_v|}} \max(\bar{p} - p_v, 0), \quad (30)$$

$$\dot{m}_{dv} = C_v (1 + \alpha_{Nuc} - \alpha^l) \frac{3\bar{\rho}^l \bar{\rho}^v}{\bar{\rho} R_B} \sqrt{\frac{2}{3\bar{\rho}^l}} \sqrt{\frac{1}{|\bar{p} - p_v|}} \min(\bar{p} - p_v, 0). \quad (31)$$

In equations (30) and (31), C_c and C_v are set to 1, p_v is the vapor

Table 1
Description of the mesh resolutions used in this paper.

Grids	n_1	n_2	n_3	n_{total}
CM	25	41	43	242k
MM	37	61	65	661K
FM	47	80	85	1623k

pressure, α_{Nuc} is the initial volume fraction of nuclei, and R_B is the radius of the nuclei which is obtained from

$$R_B = \sqrt[3]{\frac{3}{4\pi n_0} \frac{1 + \alpha_{Nuc} - \alpha^l}{\alpha^l}}. \quad (32)$$

The initial volume fraction of nuclei is calculated from

$$\alpha_{Nuc} = \frac{\frac{\pi n_0 d_{Nuc}^3}{6}}{1 + \frac{\pi n_0 d_{Nuc}^3}{6}}, \quad (33)$$

where the average number of nuclei per cubic meter of liquid volume, n_0 , and the initial nuclei diameter, d_{Nuc} , are assumed to be 10^{12} and 10^{-5} m, respectively. We remark that by selecting these values, the minimum pressure in the simulations becomes very close to the vapor pressure which mimics the equilibrium assumption made in barotropic cavitation models.

In order to discretize the convective and diffusion terms in the momentum equations, a TVD limited linear interpolation scheme, and a standard linear interpolation are, respectively, used. A first-order upwind scheme is used to discretize the convective term in the liquid fraction, and the temporal terms are discretized using a second-order implicit scheme.

3.1. Test case

In order to validate the method presented in this paper, the cavitating flow in an axisymmetric nozzle is simulated. This configuration reproduces the experiments by Franc et al. [8] in which cavitation erosion is investigated. Fig. 6a shows a schematic view of the flow configuration. The flow enters a converging nozzle, which is connected to a pipe with a diameter of 16 mm. The flow then is deflected by the plate, placed 2.5 mm away from the pipe exit, and discharges through a disk. At the edge of the pipe exit where the flow experiences a sharp turn, the pressure drops, and a sheet cavity, attached to the upper wall of the disk, forms. Fig. 6b shows the computational domain and mesh topology. The computational domain includes only 1/8 of the geometry with a symmetry boundary condition used for the side planes. The same approach is used in the numerical study by Gavaises et al. [45]. Similar to the experiments by Franc et al. [8], the flow rate at the inlet is set to 6.25 l/s and the pressure at the outlet, p_{out} is adjusted so that the cavitation number, σ , is 0.9. This cavitation number is defined as,

$$\sigma = \frac{p_{out}}{p_{in} - p_{out}}, \quad (34)$$

where p_{in} is the pressure at the inlet.

To investigate the effect of mesh resolution on the predicted erosion pattern, three grids have been created. Table 1 represents the description of these grids in the regions where the cavitation is expected to occur. In order to check whether these mesh resolutions are adequate for LES, we used the method proposed by Pope [46] where the ratio between the sub-grid scale kinetic energy and total kinetic energy is examined. For all three simulations, it was found that this ratio is smaller than 0.2 in the cavitating regions, indicating that the resolutions are enough for LES as more than 80% of total kinetic energy is resolved. In all three mesh resolutions, the averaged non-dimensional wall distance, y^+ , is around 1 while the averaged non-dimensional stream-wise distance in the cavity region, x^+ , varies from 700 to 350. The

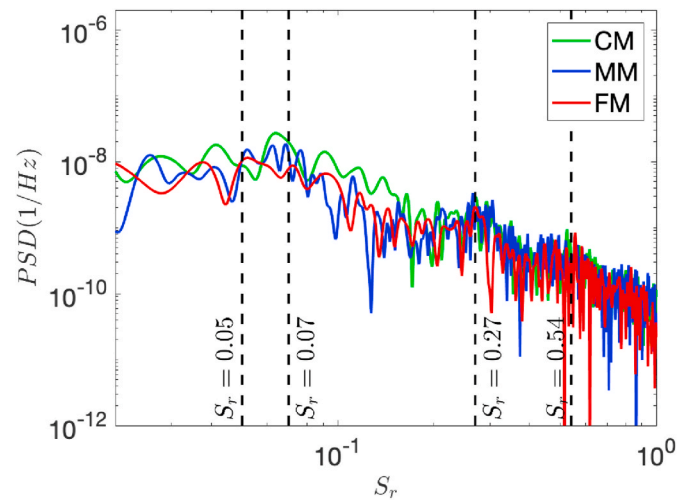


Fig. 7. Frequency spectra of the total vapor volume signal for the simulations with different mesh resolutions.

Table 2
Mean and standard deviation of the total vapor volume in the simulations with different mesh resolutions.

Simulation	$\langle V_c \rangle$	σ_{V_c}
CM	1.5×10^{-7}	4.4×10^{-8}
MM	1.9×10^{-7}	3.7×10^{-8}
FM	1.4×10^{-7}	2.2×10^{-8}

non-dimensional distance in tangential direction, z^+ , at radial location of $r = 0.015$ mm in these mesh resolutions changes between 670 and 335. It should be mentioned that this mesh resolution is not enough to capture the flow detail in the boundary layer. However, according to Franc and Michel [47], the cavity dynamics presented in this paper, i.e. unsteady sheet cavity due to re-entrant jet, is mostly inertia driven and viscous effects, such as boundary layer, do not play a role in this cavitation dynamics. For all simulations, a fixed time step is used, so that the maximum Courant number is around 1.

4. Results

Here, first the comparison of the cavity dynamics captured in the simulations with different mesh resolutions and the experiment by Gavaises et al. [45] is made. The hydrodynamic mechanisms of cavitation erosion are identified and discussed in some detail, including the flow features responsible for the erosion near the sheet inception; this has not previously been presented in the literature. The section then continues by comparing the predicted risk of cavitation erosion using the developed method and the experimental erosion pattern by Franc et al. [8], followed by discussion on the effect of mesh resolution on the predicted risk of cavitation erosion and the relation between the cavitation dynamics and the predicted risk. Lastly, the effect of simulation time and adding a threshold to the erosion risk indicator to mimic the response of material to aggressive collapse events is discussed.

The numerical results show that the cavitating flow studied in this paper exhibits an unsteady sheet cavity with periodic behaviour governed by multiple dominant frequencies. Similar observation has been made in the numerical studies by Peters et al. [20] and Mihatsch et al. [7]. To be able to compare our numerical results with similar numerical and experimental studies in literature, the dominant frequencies are expressed in term of Strouhal number which is defined as,

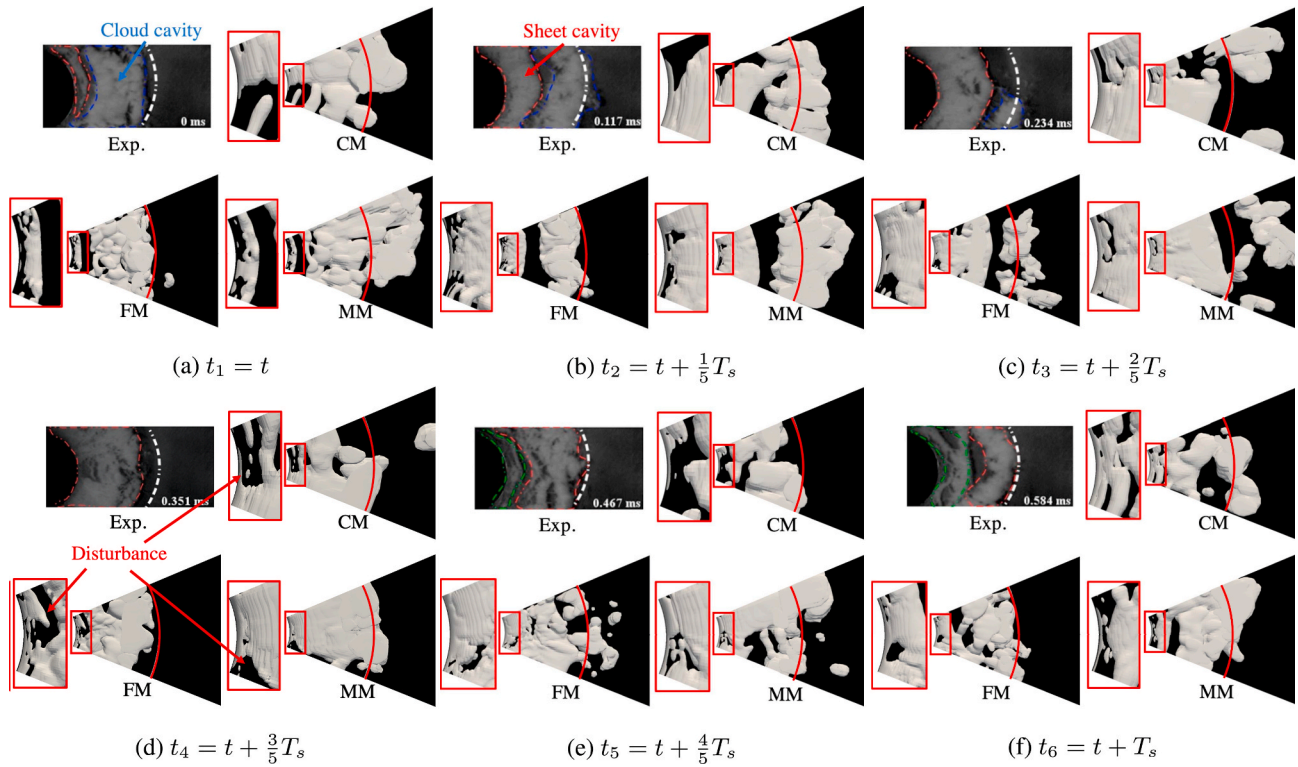


Fig. 8. Cavitation pattern in one cycle corresponding to the high dominant frequency in the numerical simulation and the experiment by Gavaises et al. [45] (The solid red lines in the simulation and dashed white lines in the experiment represent $r = 25\text{mm}$, T_s and t are, respectively, the high-frequency shedding period and the reference time, and the cavitation pattern in the simulation is shown by iso-surfaces of $\alpha^l = 0.9$). (For interpretation of the references to colour in this figure legend, the reader is referred to the Web version of this article.)

$$S_r = \frac{fL_c}{\sqrt{2(p_{in} - p_v)/\rho}} \quad (35)$$

where f is the frequency, L_c is the maximum length of the sheet cavity, and p_{in} is the inlet pressure. Fig. 7 shows the frequency spectra in the term of the Strouhal number for the simulations with three mesh resolutions, obtained by taking Fast Fourier Transform (FFT) of the history of the total vapor content in the entire domain. In all three simulations, two

dominant frequencies can be seen. The high frequency ($S_{r,h}$) is related to the periodic shedding of the cloud cavity due to the re-entrant jet. This frequency corresponds to $S_{r,h} = 0.27$ which agrees well with the numerical study by Mihatsch et al. [7] and the reported Strouhal number corresponding to unstable sheet cavity (0.25–0.35 according to Franc and Michel [47]). The harmonic of this frequency can also be seen in the frequency spectra which corresponds to $2S_{r,h} = 0.54$. The frequency spectra also shows that there exists a low dominant frequency ($S_{r,l}$) in all

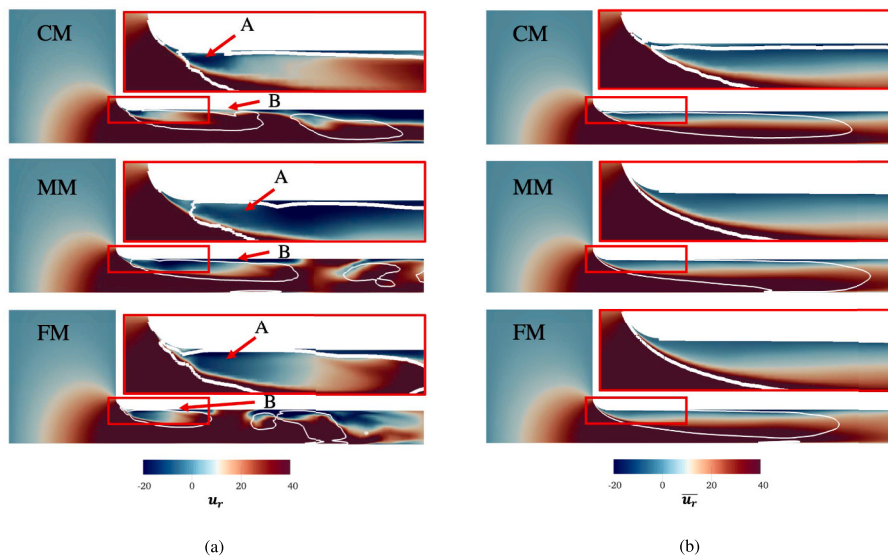


Fig. 9. Radial velocity on the tangential planes where the disturbances on the sheet cavity occur, (a) instantaneous radial velocity, (b) averaged radial velocity (The instantaneous and averaged interface of cavitating regions, shown by $\alpha^l = 0.9$ and $\bar{\alpha}^l = 0.9$, are marked by white lines).

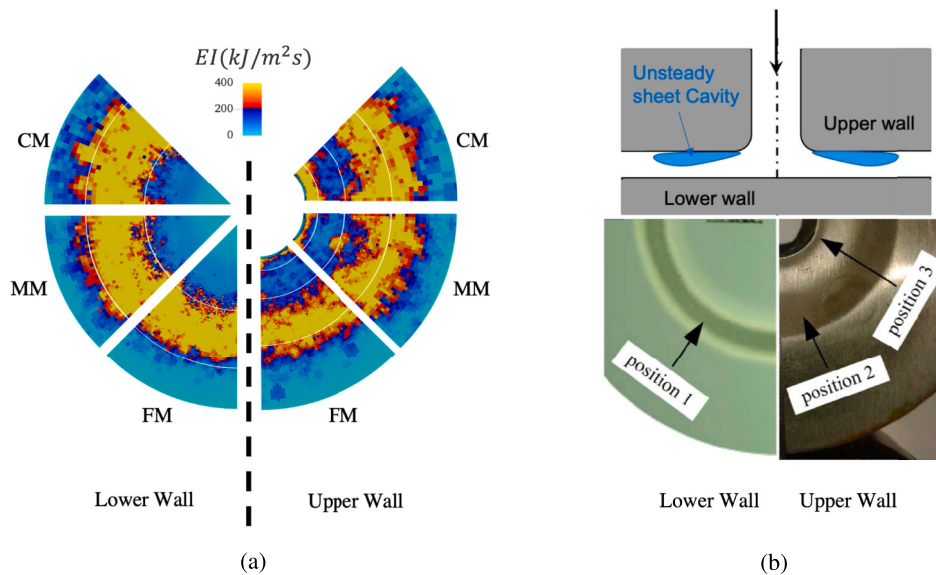


Fig. 10. Numerical and the experimental erosion pattern, (a) the predicted areas with high risk of cavitation erosion in the simulation with different mesh resolution (white lines represents the location of eroded areas in the experiment) and (b) the erosion pattern in the experiment by Franc et al. [8].

of the simulations. In contrast to the high dominant frequency, the low frequency, which corresponds to $S_{r,l} = 0.05 - 0.07$, depends on the mesh resolution. Similar mesh dependent low dominant frequency has been observed by Mihatsch et al. [7], although they identified slightly different range for this frequency ($S_{r,l} = 0.07 - 0.1$). It should be noted that the simulations by Mihatsch et al. [7] are obtained using a compressible inviscid solver, while in the present study, the simulations are viscous and based on incompressible approach. Both of these differences can explain the discrepancy between the range of the low dominant frequency in our study and the study by Mihatsch et al. [7]. Table 2 presents the mean and standard deviation of the total vapor content which are denoted, respectively, by $\langle V_v \rangle$ and σ_{V_v} . The mean value of total vapor content changes non-monotonically with the change in mesh resolution, while the standard deviation decreases by increasing mesh resolutions. This decrease is due to less cycle-to-cycle variation in the simulations with higher resolutions which will affect the sensitivity of the predicted risk to the simulation time as it will be shown later.

Fig. 8 shows the cavity dynamics in one cycle of high-frequency shedding in the present numerical simulation and the experiment by Gavaises et al. [45]. This cavity dynamics can be characterized by the following five steps. 1) $t_1 \rightarrow t_2$: A large-scale cloud cavity is formed as the sheet cavity is pinched off from the upper wall (Fig. 8a). While this cloud cavity is transported downstream by the bulk flow, a new growing sheet cavity is formed on the upper wall (Fig. 8b). 2) $t_2 \rightarrow t_3$: While the new sheet cavity is growing, cavitating structures in the shed cloud cavity collapse as they are transported downstream. Due to these collapses, the cloud cavity has become smaller in Fig. 8c. 3) $t_3 \rightarrow t_4$: The growing sheet cavity reaches its maximum length (Fig. 8d) while all of the vapor content in the cloud cavity transforms into liquid (between Fig. 8c and d). 4) $t_4 \rightarrow t_5$: An upstream moving liquid flow is formed at the end of the sheet cavity (between Fig. 8d and e). This liquid flow, often called re-entrant flow, interacts with the sheet cavity interface as it travels upstream. This interaction disturbs the interface of the sheet cavity (Fig. 8e). 5) $t_5 \rightarrow t_6$: The re-entrant flow pinches off a large scale cloud cavity from the sharp turn and a new growing sheet cavity forms on the upper wall (between Fig. 8e and f).

Note that the shedding mechanism described above have been extensively observed and studied in the cavitating flow over hydrofoils [48–50]. However, in most of these studies, the foil angle of attack is not high enough to create a separation zone at the inception region of sheet cavity while in the present flow configuration, this separation zone

occurs due to a sharp turn at the inception region as it will be shown in the paper.

The comparison between cavity dynamics in the present simulations and the experiment in Fig. 8 shows that the large-scale dynamics of the cavitating structures is qualitatively captured in comparison to the experiments on all tested meshes, although it can be noted that the CM and MM simulations are not sufficiently resolved to correctly represent all physics in the flow. This figure shows that the maximum length of the sheet cavity in CM and MM simulations is larger than in FM simulation. As this sheet cavity transforms to the cloud cavity in step $t_1 \rightarrow t_2$, the resultant cloud cavity becomes larger in the CM and MM simulations. This larger cloud cavity can then travel further downstream, leading to collapse events at larger radial distances from the pipe exit. These differences between the size of the sheet and cloud cavities and the location of the cloud cavity collapse explain the slight mesh dependency of the predicted risk of cavitation erosion obtained on the simulations with different mesh resolutions, as detailed below.

As it can be seen in the zoom-in views of Fig. 8, the interface of the sheet cavity is disturbed at the inception point near the pipe exit. An example of these disturbances is marked in Fig. 8d. The comparison between the simulations also shows that these disturbances become more significant as the mesh resolution decreases. In order to explain the cause of these disturbances and their mesh dependency, Fig. 9 presents the instantaneous and averaged radial velocity on tangential planes where the disturbances occur. In this figure, the instantaneous and the averaged interface of the cavitating regions are also shown by white lines. The distribution of the instantaneous radial velocity (Fig. 9a) shows that when the flow exits the pipe, it separates from the upper-wall due to the sharp turn. This separation zone has a high value of negative velocity (marked by A) and can be seen in all simulations; note though that some physics responsible for this separation in the CM and MM simulations should be considered only qualitatively as the mesh resolution in these simulations is coarse. Fig. 9a shows that this reverse flow is connected to a liquid reverse flow originating from the closure line of the sheet cavity (marked by B). The reverse flow marked by B supplies packets of liquid at the downstream end of the separation zone which can travel even further upstream due to the reverse flow in the separation zone. If the upstream moving liquid packets have enough momentum to reach the pipe exit, it hits the interface of the sheet cavity at the pipe exit. This collision is responsible for the disturbance on the interface of the sheet cavity seen in the zoom view in Fig. 8.

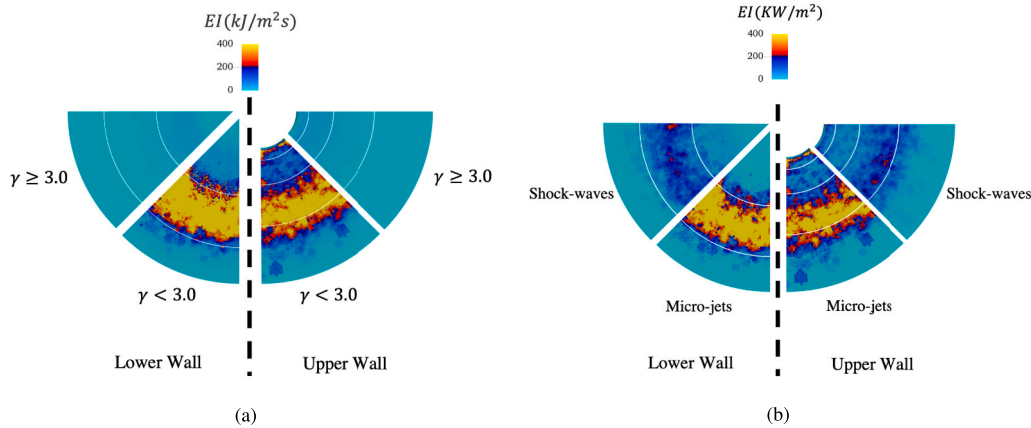


Fig. 11. Contribution of different mechanisms to the predicted risk of cavitation erosion in FM simulation, a) contribution of collapsing cavities with different stand-off distances, b) contribution of micro-jets and shock-waves to the predicted risk of cavitation erosion.

Fig. 9b shows the averaged radial velocity on the same tangential plane as Fig. 9a. A region with a negative averaged radial velocity can be seen near the wall, which indicates the presence of reverse flow in this region. The reverse flow is stronger and also thicker near the pipe exit due to the separation zone. The comparison between the zoom-in views for different simulations in Fig. 9b shows that the negative velocity of reverse flow in the separation zone decreases as the mesh resolution increases (lighter blue in zoom-in views as the mesh resolution increases). As mentioned above, the combined effect of this reverse flow in the separation zone and the reverse flow at the closure line of the sheet cavity leads to the disturbance on the sheet cavity near the pipe. Therefore it is expected that the disturbances are more significant in the CM simulation compared to the MM and FM simulations.

Fig. 10 compares the experimental erosion pattern by Franc et al. [8] and the areas with high risk of cavitation erosion identified by the developed method. In the experiment, erosion can be seen in three main regions, a region on the lower wall with the radial extension $19 \text{ mm} < r < 32 \text{ mm}$, a region on the upper wall with the radial extension $17 \text{ mm} < r < 27 \text{ mm}$, and a region on the upper wall between the pipe exit and $r = 11 \text{ mm}$. These regions are shown in Fig. 10b, respectively, by position 1 to 3, and their radial extension are marked by white lines in the numerical results. The comparison between the numerical results in Fig. 10 shows that regardless of the mesh resolution, the presented method predicts the areas with high risk of cavitation erosion, which are qualitatively comparable with the experimental erosion pattern. It is also seen that the change in the mesh resolution slightly affects the radial extension of 1 and 2 as well as the location of position 2. By increasing the mesh resolution, the radial extension of positions 1 and 2 decreases, and the location of position 2 slightly shifts toward lower

radial locations. These differences are due to the larger sheet and cloud cavities in CM and MM simulations which is shown in Fig. 8. Slightly higher mesh dependency can be seen in position 3 where the predicted area with high erosion risk reduces progressively by increasing mesh resolution.

Fig. 11a shows the risk of cavitation erosion associated with the collapse of cavities with different stand-off ratios. It can be seen that the contribution of collapsing cavities with the stand-off ratio equal to or larger than 3 to the predicted risk of cavitation erosion is insignificant. As mentioned in section 2, the kinetic energy in the surrounding liquid of these collapsing cavities is assumed to be converted to acoustic energy in shock-waves. As these collapse events are far away from the surface and the acoustic energy of the shock-wave decays with the distance, the absorbed energy by surface due to the impacts of these shock-waves is expected to be small. Fig. 11b shows the contribution of different mechanisms of cavitation erosion, micro-jets and shock-waves, to the predicted risk of cavitation erosion. It can be seen that although the contribution of shock-waves are smaller compared to the contribution of micro-jets, the contribution of these two mechanisms are in the same order, which highlights the importance of considering both mechanisms in the numerical methods predicting the risk of cavitation erosion. We remark that our findings presented here are inline with the description of cavitation erosion by Dular and Coutier-Delgosha [51]. In this description, it is assumed that the contribution of shock-waves due to the collapse of cavities away from the surface is small, which corresponds well with the results presented in Fig. 11a. Further, the description of cavitation erosion by these authors assumes that these shock-waves can trigger the collapse of bubbles near the surface which can cause erosion through micro-jets. In present study, this acoustic

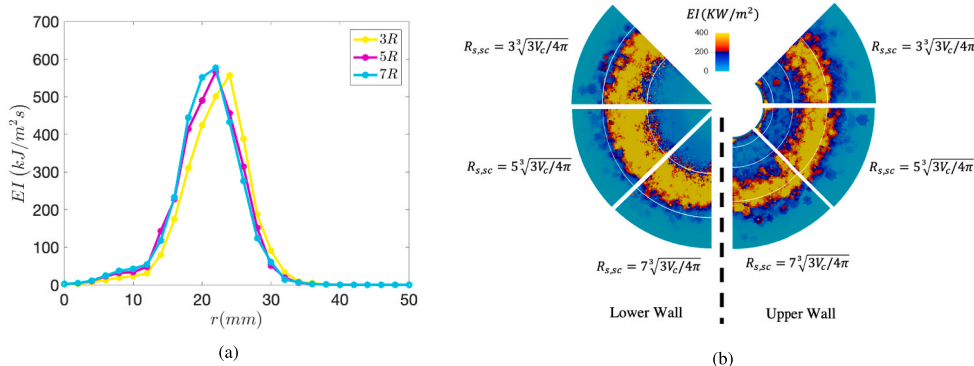


Fig. 12. Effect of the choice of the radius $R_{s,sc}$ on the predicted risk of cavitation erosion, a) radial distribution of erosion indicator on the lower wall, b) predicted areas with high risk of cavitation erosion on the lower and upper wall.

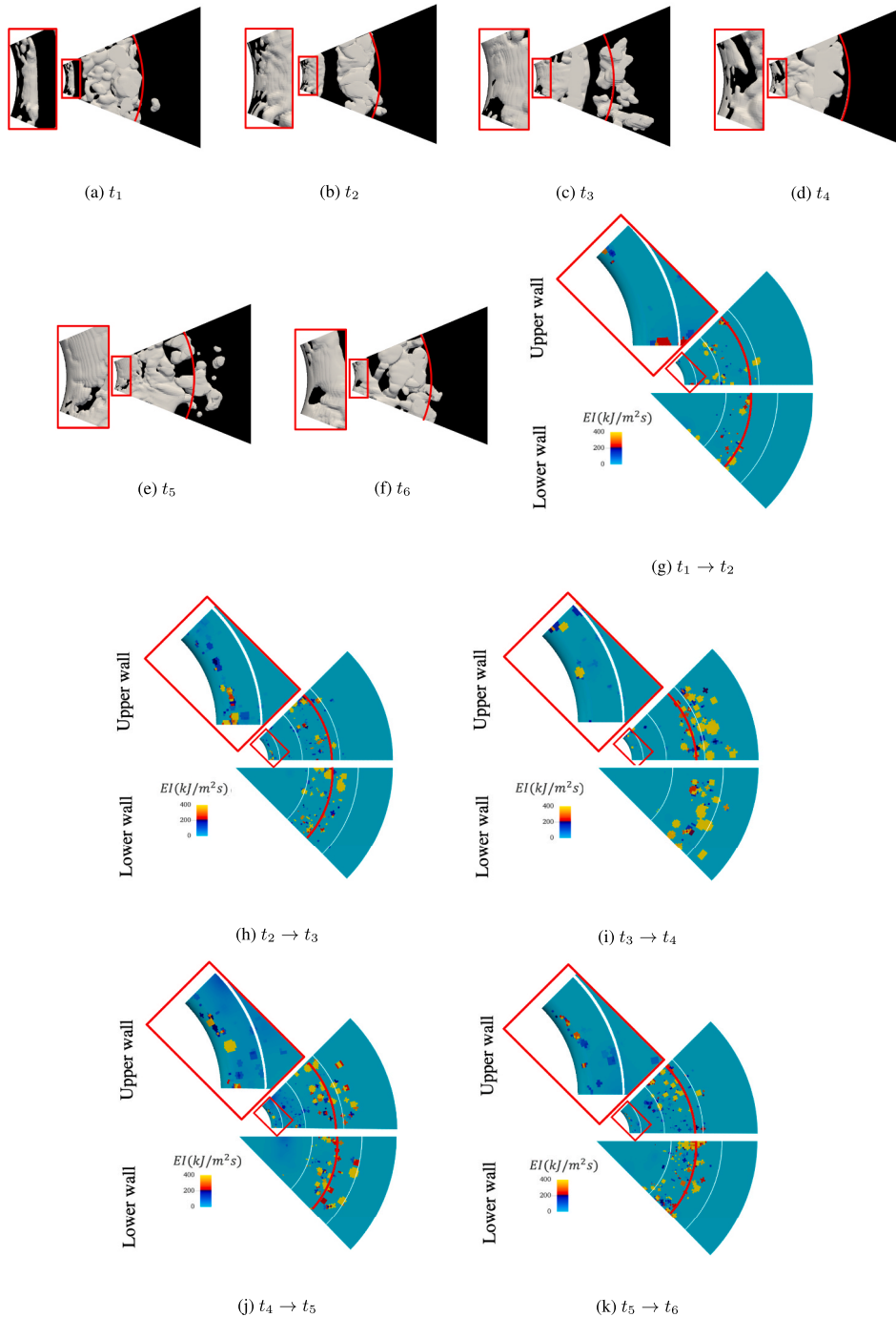


Fig. 13. Hydrodynamic mechanism of cavitation erosion risk, a-f) steps in the cavity dynamics (The solid red lines represent $r = 25\text{mm}$ and the white lines represent the eroded region in the experiment). (For interpretation of the references to colour in this figure legend, the reader is referred to the Web version of this article.)

interaction is considered in the cavities with $0 < \gamma < 3.0$. It is assumed that a number of bubbles in these cloud cavities which are away from the surface produce shock-waves. A portion of the acoustic energy carried by these shock-waves is then assumed to be transferred to bubbles near the surface which in turn can cause erosion through the micro-jet mechanism.

As described in section 2.1, the proposed numerical method requires the splitting of the liquid volume around collapsing cavities into near-field and far-field volumes. The near-field volume is the liquid inside a sphere or spherical cap with radius of $R_{s,sc}$. For the results presented so far in this section, this radius is selected to be five times larger than the

radius of the sphere with the same volume of the collapsing cavity. In order to investigate the effect of this selection on the predicted risk of cavitation erosion, the results from two extra simulations are presented here. In these simulations which are performed on the fine mesh, the radius $R_{s,sc}$ is assumed to be 3 and 7 times larger than the cloud volume-equivalent radius. Fig. 12a shows the radial distribution of the predicted erosion risk on the lower wall using the three values of $R_{s,sc}$. It can be seen that the predicted risk of cavitation erosion using $R_{s,sc} = 3\sqrt[3]{(3V_c/4\pi)}$ is slightly shifted toward larger radial positions compared to the predicted risk using the other two values of $R_{s,sc}$. Further, the

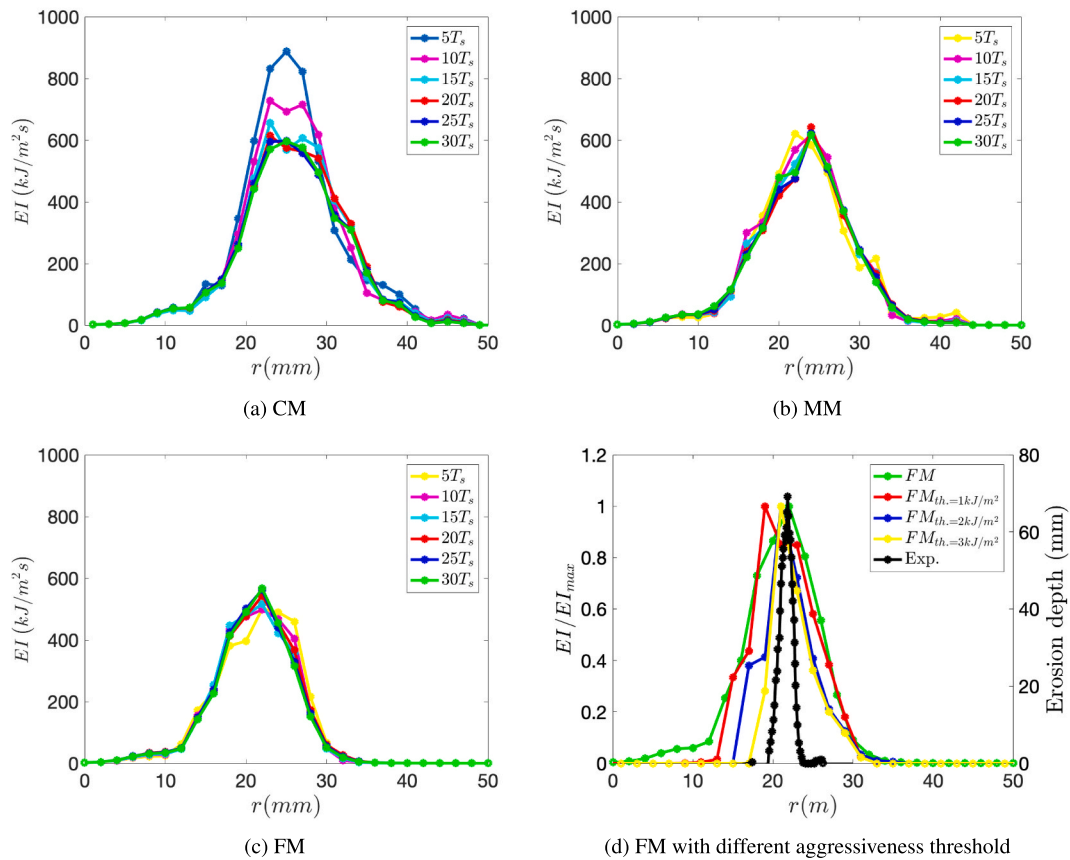


Fig. 14. Distribution of the erosion indicator on the lower wall obtained using different simulation times and mesh resolution. mesh resolutions and the distribution of the erosion depth in the experiment by Franc et al. [8].

radial extension of the predicted risk using $R_{s,sc} = 3\sqrt[3]{(3V_c/4\pi)}$ is slightly smaller. However, the comparison between the erosion assessment using $R_{s,sc} = 5\sqrt[3]{(3V_c/4\pi)}$ and $R_{s,sc} = 7\sqrt[3]{(3V_c/4\pi)}$ shows that this assessment is the same in these two simulations. The maximum risk of cavitation erosion in these simulations occurs in the same radial location and the radial extension of the predicted erosion risk is almost the same. Fig. 12b presents the areas with high risk of cavitation erosion on the lower and upper wall using the three values of $R_{s,sc}$. The comparison in this figure shows that the predicted high-risk areas are qualitatively the same in the simulations with different values $R_{s,sc}$. From this comparison, it can be concluded that the areas with high risk of cavitation erosion predicted by the developed method are not sensitive to the choice of $R_{s,sc}$.

Fig. 13 shows the steps in cavitation dynamics as well as their associated risk of cavitation erosion for one shedding cycle in FM simulation. It can be seen in this figure that the risk of cavitation erosion in position 1 and 2, shown in Fig. 10, is not restricted to the cavity dynamics in a specific step. In the step $t_1 \rightarrow t_2$ (Fig. 13a \rightarrow Fig. 13b), as the detached cloud rolls downstream, aggressive collapse events occur in its upstream and downstream ends which induce a high risk of cavitation erosion on both walls (Fig. 13g). More aggressive collapse events can be seen in the step $t_2 \rightarrow t_3$ (Fig. 13b \rightarrow Fig. 13c) when the cloud cavity travels further downstream and starts to shrink. In the step $t_3 \rightarrow t_4$ (Fig. 13c \rightarrow Fig. 13d), the traveling cloud suddenly collapses leading to a high risk of cavitation erosion on both walls. The comparison between the erosion risk in this step and in other steps indicates that this large-scale collapse of the cloud cavity is associated with the highest risk of cavitation erosion compared to the other collapse events in the cycle. During the steps $t_1 \rightarrow t_4$, a new sheet cavity appears and grows to its maximum length which can be seen in Fig. 13d. In the step $t_4 \rightarrow t_5$, a re-entrant jet forms at

the downstream end of the sheet cavity. According to Arabnejad et al. [42], the interaction between this re-entrant jet and the downstream end of the sheet cavity leads to the detachment of cavity structures. Similar detachment of cavity structures can be seen in Fig. 13e. These structures can collapse due to high-pressure around the closure line and produce a high risk of cavitation erosion as it can be seen in Fig. 13j. In step $t_5 \rightarrow t_6$ (Fig. 13e \rightarrow Fig. 13f), the re-entrant jet reaches the region near the pipe exit and pinches off a cloud cavity from the upper wall. Fig. 13k shows that in this step, collapse events occur underneath and on the top of the detached cavity which can cause a high risk of cavitation erosion on both walls.

The steps in cavitation dynamics and its associated risk of cavitation erosion in the position 3, shown in Fig. 10, are presented in the zoom-in views in Fig. 13. Comparison between the locations of high erosion risk and cavity dynamics indicates that the high risk of cavitation erosion occurs mostly in the region where there is a disturbance in the interface of the sheet cavity near the pipe exit. At the location of these disturbances as shown in Fig. 9, there is a liquid reverse flow augmented by the separation zone. When this liquid reverse flow reaches the pipe exit, it hits the flow exiting the pipe. This collision can increase the pressure locally leading to aggressive collapse events in the pipe exit which are responsible for the high risk of cavitation erosion in position 3.

Fig. 14 shows the tangentially averaged distribution of the erosion risk indicator, EI , on the lower wall in the simulations with different mesh resolutions. These distributions are obtained using different simulation times in order to investigate the effect of this parameter. It can be seen that the distribution of EI in all three simulations does not change significantly if the simulation time is larger than 20 shedding periods, T_s . However, the sensitivity of this distribution to the simulation times smaller than $20T_s$ is not the same in the simulations with

different mesh resolutions. This sensitivity is higher in CM simulation compared to MM and FM simulations which can be due to higher cycle-to-cycle variation in CM simulation as shown in Table 2. Comparison between converged distributions of EI ($t \geq 20T_s$) in all simulations also shows that the maximum value of EI is not mesh dependent while the radial location of this maximum value and the extent of erosion risk slightly depend on the mesh resolution. As discussed earlier, this mesh dependency is due to a different dynamics of sheet and cloud cavities in the simulations with different mesh resolutions. Fig. 14d compares the converged distribution of EI in FM simulation (green line) with the erosion depth profile in the experiment by Franc et al. [8]. It can be seen that the radial extension of EI distribution is quite larger than the extension of the erosion depth profile. This discrepancy is due to the definition of the erosion indicator in equation (21) which do not consider the response of material to the absorbed energy. Due to this deficiency, the energy transferred to the surface elements by all of the collapse events contributes to the risk of cavitation erosion while the amount of this transferred energy for some collapse events might not be high enough to cause erosion. To consider only the effect of highly aggressive events, one can modify the definition of the erosion indicator as,

$$EI_j = \frac{1}{V_s} \sum_{i=1}^{n_i} \begin{cases} \frac{E_{mat.-j,i}}{A_j} & \frac{E_{mat.-j,i}}{A_j} > th. \\ 0 & \frac{E_{mat.-j,i}}{A_j} \leq th. \end{cases}, \quad (36)$$

where $th.$ is the threshold above which the absorbed energy per area is high enough to cause erosion. Obtaining this threshold as a function of the material properties is a subject of future work. However, to show that adding a threshold to the definition of the erosion indicator can improve the results, Fig. 14d presents the distribution of the modified erosion indicator for different values of threshold. The distributions are normalized by their maximum values to able to show them in one figure. It can be seen that by increasing the threshold, the extension of the estimated risk of erosion becomes closer to the experimental erosion depth profile.

5. Conclusions

This paper presents a new method to assess the risk of cavitation erosion using incompressible simulations of cavitating flows. The method is based on the energy balance between the cavitating structures and cavitation erosion suggested by Hammitt [23]. In contrast to previous methodologies [24,27,34] in which the potential energy of collapsing cavities has been used for erosion assessment, the presented method uses the kinetic energy in the surrounding liquid to estimate the risk of cavitation erosion. The developed method then estimates how to this kinetic energy is transfer to the surface through two well-known mechanisms of cavitation erosion, shock-waves and micro-jets.

In order to validate the method, the cavitating flow in a stagnation nozzle flow is simulated using three mesh resolutions, and the areas with predicted high risk of cavitation erosion are compared with the erosion pattern in the experiment by Franc et al. [8]. It is shown that regardless of mesh resolution, the predicted areas with high erosion risk are qualitatively in good agreement with the experiment. The agreement with the experimental results improves with mesh resolution due to an improved prediction of the cavity extent and dynamics on the finer mesh.

Using the proposed method, the relationship between the cavity dynamics and the risk of cavitation erosion at the inception region of the sheet cavity is investigated. It is shown that the high risk of cavitation erosion in this region is closely related to the separation zone in this region. Due to this separation zone, the reverse liquid flow underneath the sheet cavity gains momentum and hits the flow exiting the pipe which increases the pressure locally. This high pressure can trigger

collapse events with high risk of cavitation erosion near the inception region of the sheet cavity.

The results presented in this paper show that the proposed method is able to identify areas with high risk of cavitation erosion in a simple geometry such as an axisymmetric nozzle. In order to examine this capability in geometries relevant to marine applications, the proposed method will be applied to the cavitating flows in a commercial water jet pump and the results will be compared with the experimental erosion assessment as the future work.

Author statement

Mohammad Hossein Arabnejad: Conceptualization, Methodology, Software, Validation, Investigation, Writing-Original Draft, Visualization, **Urban Svennberg:** Supervision, Writing- Reviewing and Editing, **Rickard E. Bensow:** Supervision, Writing- Reviewing and Editing, Funding acquisition.

Declaration of competing interest

The authors declare that they have no known competing financial interests or personal relationships that could have appeared to influence the work reported in this paper.

Acknowledgments

Financial support for this work has been provided by the EU H2020 Project CaFE, a Marie Skłodowska-Curie Action Innovative Training Network Project, grant number 642536, and Kongsberg Maritime through the University Technology Center in Computational Hydrodynamics hosted at the Division of Marine Technology, Department of Mechanics and Maritime Sciences at Chalmers. The authors would like also thank Dr. Abolfazl Asnaghi for his insightful comments on the manuscript. The simulations were performed on resources provided by Chalmers Center for Computational Science and Engineering (C3SE).

References

- [1] G. Bark, N. Berchiche, M. Grekula, Application of Principles for Observation and Analysis of Eroding Cavitation-The EroCav Observation Handbook, EROCAV Report, Dept. of Naval Architecture, Chalmers University of Technology, Göteborg, Sweden, 2004.
- [2] M. Van Rijsbergen, E. Foeth, P. Fitzsimmons, A. Boorsma, High-speed video observations and acoustic-impact measurements on a NACA0015 foil, in: Proceedings of the 8th International Symposium on Cavitation, 2012. Singapore.
- [3] W. Pfitsch, S. Gowing, D. Fry, M. Donnelly, S. Jessup, Development of measurement techniques for studying propeller erosion damage in severe wake fields, in: 7th International Symposium on Cavitation, 2009. Michigan, USA.
- [4] Y. Cao, X. Peng, K. Yan, L. Xu, L. Shu, A qualitative study on the relationship between cavitation structure and erosion region around a 3d twisted hydrofoil by painting method, in: Fifth International Symposium on Marine Propulsors, Finland, 2017.
- [5] P. Koukouvinis, N. Mitroglou, M. Gavaises, M. Lorenzi, M. Santini, Quantitative predictions of cavitation presence and erosion-prone locations in a high-pressure cavitation test rig, J. Fluid Mech. 819 (2017) 21–57.
- [6] F. Örlay, S. Hickel, S.J. Schmidt, N.A. Adams, Large-eddy simulation of turbulent, cavitating fuel flow inside a 9-hole diesel injector including needle movement, Int. J. Engine Res. 18 (3) (2017) 195–211.
- [7] M. Mihatsch, S. Schmidt, N. Adams, Cavitation erosion prediction based on analysis of flow dynamics and impact load spectra, Phys. Fluids 27 (10) (2015) 103302.
- [8] J. Franc, M. Riondet, A. Karimi, G.L. Chahine, Impact load measurements in an erosive cavitating flow, J. Fluid Eng. 133 (12) (2011), 121301.
- [9] M. Blume, R. Skoda, 3d flow simulation of a circular leading edge hydrofoil and assessment of cavitation erosion by the statistical evaluation of void collapses and cavitation structures, Wear 428 (2019) 457–469.
- [10] B. Budich, S. Schmidt, N. Adams, Numerical investigation of a cavitating model propeller including compressible shock wave dynamics, in: Fourth International Symposium on Marine Propulsors, 2015. Texas, USA.
- [11] B. Budich, S. Schmidt, N. Adams, Numerical simulation of cavitating ship propeller flow and assessment of erosion aggressiveness, in: Fourth International Symposium on Marine Propulsors, 2015. Texas, USA.
- [12] M.H. Arabnejad, A. Amiri, M. Farhat, R.E. Bensow, Hydrodynamic mechanisms of aggressive collapse events in leading edge cavitation, J. Hydrodyn. 32 (1) (2020) 6–19.

- [13] N. Ochiai, Y. Iga, M. Nohmi, T. Ikohagi, Study of quantitative numerical prediction of cavitation erosion in cavitating flow, *J. Fluid Eng.* 135 (1) (2013), 011302.
- [14] A. Peters, O. el Moctar, Numerical assessment of cavitation-induced erosion using a multi-scale euler-lagrange method, *J. Fluid Mech.* 894 (2020).
- [15] L. Krumenacker, R. Fortes-Patella, A. Archer, Numerical estimation of cavitation intensity, in: *IOP Conference Series: Earth and Environmental Science*, vol. 22, 2014, 052014.
- [16] Z. Li, M. Pourquie, T. van Terwisga, Assessment of cavitation erosion with a urans method, *J. Fluid Eng.* 136 (4) (2014), 041101.
- [17] C. Eskilsson, R.E. Bensow, Estimation of cavitation erosion intensity using CFD: numerical comparison of three different methods, in: *Fourth International Symposium on Marine Propulsors*, 2015. Texas, USA.
- [18] P. Koukouvini, G. Bergeles, A cavitation aggressiveness index within the Reynolds averaged Navier Stokes methodology for cavitating flows, *J. Hydrodyn.* 27 (4) (2015) 579–586.
- [19] M. Dular, B. Stoffel, B. Širok, Development of a cavitation erosion model, *Wear* 261 (5–6) (2006) 642–655.
- [20] A. Peters, H. Sagar, U. Lantermann, O. el Moctar, Numerical modelling and prediction of cavitation erosion, *Wear* 338 (2015) 189–201.
- [21] A. Peters, U. Lantermann, O. el Moctar, Numerical prediction of cavitation erosion on a ship propeller in model-and full-scale, *Wear* 408 (2018) 1–12.
- [22] T. Van, P. Fitzsimmons, E. Foeth, Z. Li, Cavitation erosion: a critical review of physical mechanisms and erosion risk models. 7th International Symposium on Cavitation, 2009. Michigan, USA.
- [23] F.G. Hammit, Observations on cavitation damage in a flowing system, *J. Fluid Eng.* 85 (3) (09 1963) 347–356, 0098–2202.
- [24] R. Fortes-Patella, J. Reboud, L. Briancon-Marjollet, A phenomenological and numerical model for scaling the flow aggressiveness in cavitation erosion, in: *EROCV Workshop*, Val de Reuil, France, vol. 11, 2004, pp. 283–290.
- [25] S. Schenke, T. Melissaris, T. van Terwisga, On the relevance of kinematics for cavitation implosion loads, *Phys. Fluids* 31 (5) (2019), 052102.
- [26] R. Fortes-Patella, A. Archer, C. Flageul, Numerical and experimental investigations on cavitation erosion, in: *IOP Conference Series: Earth and Environmental Science*, vol. 15, IOP Publishing, 2012, 022013.
- [27] T. Melissaris, N. Bulten, T. van Terwisga, On the applicability of cavitation erosion risk models with a urans solver, *J. Fluid Eng.* 141 (10) (2019), 101104.
- [28] T. Melissaris, S. Schenke, N. Bulten, T.J.C. van Terwisga, On the Accuracy of Predicting Cavitation Impact Loads on Marine Propellers, *Wear*, 2020, 203393.
- [29] A. Vogel, W. Lauterborn, Acoustic transient generation by laser-produced cavitation bubbles near solid boundaries, *J. Acoust. Soc. Am.* 84 (2) (1988) 719–731.
- [30] R. Fortes-Patella, G. Challier, J. Reboud, A. Archer, Energy balance in cavitation erosion: from bubble collapse to indentation of material surface, *J. Fluid Eng.* 135 (1) (2013), 011303.
- [31] A. Vallier, Simulations of Cavitation - from the Large Vapour Structures to the Small Bubble Dynamics, PhD thesis, Lund University, 2013.
- [32] D. Silver, X. Wang, Tracking and visualizing turbulent 3D features, *IEEE Trans. Visual. Comput. Graph.* 3 (2) (1997) 129–141.
- [33] C. Leclercq, A. Archer, R. Fortes-Patella, F. Cerru, Numerical cavitation intensity on a hydrofoil for 3d homogeneous unsteady viscous flows, *International Journal of Fluid Machinery and Systems* 10 (3) (2017) 254–263.
- [34] S. Schenke, T. van Terwisga, An energy conservative method to predict the erosive aggressiveness of collapsing cavitating structures and cavitating flows from numerical simulations, *Int. J. Multiphas. Flow* 111 (2019) 200–218.
- [35] E. Johnsen, T. Colonius, Numerical simulations of non-spherical bubble collapse, *J. Fluid Mech.* 629 (2009) 231–262.
- [36] M. Dular, J. Požar, T. Zevnik, et al., High speed observation of damage created by a collapse of a single cavitation bubble, *Wear* 418 (2019) 13–23.
- [37] J. Ma, C. Hsiao, G.L. Chahine, Euler-Lagrange simulations of bubble cloud dynamics near a wall, *J. Fluid Eng.* 137 (4) (2015).
- [38] T. Okada, Y. Iwai, S. Hattori, N. Tanimura, Relation between impact load and the damage produced by cavitation bubble collapse, *Wear* 184 (2) (1995) 231–239.
- [39] H.G. Weller, G. Tabor, H. Jasak, C. Fureby, A tensorial approach to computational continuum mechanics using object-oriented techniques, *Comput. Phys.* 12 (6) (1998) 620–631.
- [40] R.E. Bensow, G. Bark, Implicit LES predictions of the cavitating flow on a propeller, *J. Fluid Eng.* 132 (4) (2010), 041302.
- [41] A. Asnaghi, A. Feymark, R.E. Bensow, Improvement of cavitation mass transfer modeling based on local flow properties, *Int. J. Multiphas. Flow* 93 (2017) 142–157.
- [42] M.H. Arabnejad, A. Amini, R.E. Bensow, M. Farhat, Numerical and experimental investigation of shedding mechanisms from leading-edge cavitation, *Int. J. Multiphas. Flow* 119 (2019) 123–143.
- [43] F. Nicoud, F. Ducros, Subgrid-scale stress modelling based on the square of the velocity gradient tensor, *Flow, Turbul. Combust.* 62 (3) (1999) 183–200.
- [44] J. Sauer, Instationär kavitierende strömungen-ein neues modell, basierend auf front capturing (vof) und blasendynamik, Diss., Uni Karlsruhe, 2000.
- [45] M. Gavaises, F. Villa, P. Koukouvini, M. Marengo, J. Franc, Visualisation and LES simulation of cavitation cloud formation and collapse in an axisymmetric geometry, *Int. J. Multiphas. Flow* 68 (2015) 14–26.
- [46] S.B. Pope, *Turbulent Flows*, Cambridge University Press, 2000, <https://doi.org/10.1017/CBO9780511840531>.
- [47] J. Franc, J. Michel, *Fundamentals of Cavitation*, vol. 76, Springer Science & Business Media, 2006.
- [48] E. Foeth, T. van Terwisga, C. van Doorne, On the collapse structure of an attached cavity on a three-dimensional hydrofoil, *J. Fluid Eng.* 130 (7) (2008), 071303.
- [49] M. Callenaere, J. Franc, J. Michel, M. Riondet, The cavitation instability induced by the development of a re-entrant jet, *J. Fluid Mech.* 444 (2001) 223–256.
- [50] K. Laberteaux, S. Ceccio, Partial cavity flows. part 1. cavities forming on models without spanwise variation, *J. Fluid Mech.* 431 (2001) 1–41.
- [51] M. Dular, O. Coutier-Delgosha, Numerical modelling of cavitation erosion, *Int. J. Numer. Methods Fluid.* 61 (12) (2009) 1388–1410.